Carbon 181 (2021) 193–203

Contents lists available at ScienceDirect

Carbon

journal homepage: www.elsevier.com/locate/carbon

Research Article

Disordered nitrogen-defect-rich porous carbon nitride photocatalyst for highly efficient H_2 evolution under visible-light irradiation

Cheng Cheng [a], Jinwen Shi [a, *], Linyuan Wen [a], Chung-Li Dong [b], Yu-Cheng Huang [b], Yazhou Zhang [a], Shichao Zong [a], Zhidan Diao [a], Shaohua Shen [a], Liejin Guo [a]

[a] International Research Center for Renewable Energy (IRCRE), State Key Laboratory of Multiphase Flow in Power Engineering (MFPE), Xi'an Jiaotong University (XJTU), 28 West Xianning Road, Xi'an, 710049, PR China
[b] Department of Physics, Tamkang University, 151 Yingzhuan Road, Tamsui, 25137, Taiwan

ARTICLE INFO

Article history:
Received 23 February 2021
Received in revised form
8 May 2021
Accepted 10 May 2021
Available online 18 May 2021

Keywords:
Disordered structure
Defect
Hydrogen
Photocatalysis
Solar energy

ABSTRACT

Precursor types play crucial factors for synthesizing high-efficiency graphitic carbon nitrides (GCNs). Herein, biuret was employed as a new precursor to prepare a disordered nitrogen-defect-rich porous GCN (BCN). The crystallinity, structure and performance properties for BCN were explored by making systematic comparisons with other commonly available GCNs which were derived from conventional precursors under the identical conditions. Biuret could be the optimal choice for the preparation of high-performance GCN according to the reports so far. BCN not only possessed long-range atomic disordered structure, but also contained numerous nitrogen defects embedded into the in-planes of the disordered GCN networks, leading to extended visible-light absorption (absorption edge at 525 nm), improved separation of photoexcited charge carriers, and rich available reactive sites. The large surface area and high porosity of BCN also provided plenty of reactive sites. Consequently, ultrahigh photocatalytic H_2 production and excellent O_2 production performance were achieved for BCN, the AQY for H_2 production achieved 45.5% at 420 nm, which was one of the highest values for GCN-based photocatalysts.

1. Introduction

Semiconductor-based photocatalysis has been widely regarded as one of the attractive avenues to convert inexhaustible and clean solar energy in the form of green sustainable chemical energy (H_2) [1,2]. The feasible technology gains considerable interdisciplinary attentions due to its diversely potential application in environmental and energy crisis. By following the fact that the visible light occupies energy about 43% in the whole solar spectrum, it is definite that developing available visible-light-responsive photocatalysts is pivotal to realize the target of high-efficient photocatalysis for H_2 evolution [3–5]. Among lots of reported photocatalysts, graphitic carbon nitrides (GCNs), as one type of fascinating conjugated polymer, emerge as shining stars and perform outstandingly in the field of photocatalytic H_2 production due to the significant merits of "earth-abundant" nature, appealing electronic properties and specific planar structure, which lead to favorable properties of low-cost, visible-light response, non-toxic, good chemical stability and tunable band structure [6–9].

However, practical applications of pristine GCNs are still seriously restricted by the low photocatalytic H_2-production efficiency, which usually caused by several obstacles and shortcomings, including limited absorption range of visible-light, high recombination rate of photo-generated charge carriers and low electrical conductivity [10–12]. To address these limitations, numerous strategies have been developed to improve the chemical and physical properties of GCNs for enhancing the photocatalytic performance, such as doping with heteroatoms (e.g., C, N, B, O, S, P, and Cu) [13–20], copolymerization [21,22], morphology design [23,24], introducing defects [25], crystallizing the GCNs [26], and exfoliation to a few layers [27]. As a matter of fact, the formation of pristine GCNs directly from precursor plays a pivotal role as footstone in the above strategies, the pristine GCNs derived from different precursors usually possess similar crystal structure but diverse photocatalytic activities. Basically and importantly, the precursor types and reaction conditions are crucial factors for synthesizing GCNs, they have influence on the physicochemical properties of the resultant GCNs, such as C/N ratio, degree of

* Corresponding author.
E-mail address: jinwen_shi@mail.xjtu.edu.cn (J. Shi).

https://doi.org/10.1016/j.carbon.2021.05.030
0008-6223/

crystallinity and polymerization, light absorption capacity, porosity, specific surface area, and micro-nano morphology. According to the reports, GCNs can be easily fabricated by thermal polymerization of the nitrogen-rich precursors which contain C=N core structures, such as melamine, thiourea, dicyandiamide, or urea and so forth [28–31], exploration of new precursor materials for GCNs preparation has always been put forward as an effective strategy for preparing high-efficiency GCNs.

The degree of order in long-range atomic arrangements determines the crystallinity of GCNs and greatly influences the structure and property. Interestingly, disordered materials have unique atomic arrangements of long-range disorder but short-range order, resulting in distinct electronic, optical, magnetic and mechanical properties [32–34]. The distortion originated from the disordered structure of GCNs can allow and activate more $n \rightarrow \pi^*$ electron transitions to enhance the optical properties with the appearance of new visible light absorption beyond 460 nm [18,19]. What's more, disordered structure of GCNs is usually accompanied by the introduction of defects, which could function to regulate the band structure for enhancing visible-light absorption and work as reactive sites for photocatalytic reaction [7,35,36]. For example, Kang et al. synthesized amorphous carbon nitride with a narrow band gap (1.9 eV) via a strategy of postheating the partially crystalline GCN at a high temperature (620 °C) [37]. However, there is rare report about preparation of disordered GCNs directly from precursor material.

During all the reported precursors, urea is preferred as the optimal material for conversion into sheet-like GCNs with excellent photocatalytic H_2-production performance. Significantly, for the synthetic process of the urea-derived GCNs, the oxygen species can promote the connectivity and packing of GCN sheets, accelerate the polymerization/condensation process, enable structural perfection as well as enhance delocalization of electrons in aromatic sheets, resulting in promoted the photocatalytic redox functions [31,38]. Meanwhile, the oxygen species do not participate in constructing the GCN networks and act as additional leaving motifs in the form of gases (like NO_x), leading to high porosity and high specific surface area. Inspired by the structure and composition of urea, another oxygen-containing compound: biuret, which is the downstream product of urea, can be predicted as a new precursor to form GCN networks by undergoing self-polymerization and condensation (Fig. S1). Herein, biuret was employed to prepare porous nitrogen-defect-rich disordered graphitic carbon nitride by the direct thermal polymerization method, as depicted schematically in Fig. 1. Other GCNs samples derived from conventional precursors (melamine, dicyandiamide, thiourea and urea) were also synthesized under identical conditions. With making systematic comparisons of BCN and other GCNs samples, the electronic and textural structure characteristics of BCN were analyzed to demonstrate the inherent reasons for the ultrahigh photocatalytic H_2 production activity.

2. Experimental section

2.1. Preparation of GCNs

GCNs was prepared via the commonly used direct thermal polymerization of organic precursors. In details, biuret, urea, thiourea, dicyandiamide, and melamine (each 1 g) as precursors were transferred into clean alumina crucibles with covers, respectively, and then calcined at 550 °C (ramping rate, 5 °C min^{-1}) for 4 h under Ar atmosphere. After cooling down to room temperature, the corresponding powders were collected for photocatalysts and denoted as BCN, UCN, TCN, DCN and MCN, respectively. In addition, biuret powder (1 g) also calcined at other temperature (520 and 600 °C) in the similar procedure, and the final products denoted as BCN−520 and BCN−600, respectively.

Characterization and *Photoelectrochemical measurement* were provided in the Supplementary Material.

2.2. Photocatalytic measurement

Photocatalytic H_2 and O_2 production were performed in a sealed Pyrex glass reactor (120 mL) in which light irradiated from the side window. A Xe lamp (300 W) equipped with a UV-cutoff filter ($\lambda > 420$ nm) was used as the visible-light source (Fig. S2). For the photocatalytic H_2 production, triethanolamine (TEOA) functioned as sacrificial agent to consume photo-generated holes. In detail, photocatalysts (10 mg), TEOA (8 mL) and deionized water (72 mL) were mixed into the glass reactor with stirring. Pt (3 wt%) as cocatalyst was photodeposited in situ on photocatalyst with $H_2PtCl_6 \cdot 6H_2O$ as precursor. In addition, photocatalytic H_2-evolution reactions were also performed in the similar photocatalytic system except using formic acid (10 vol%), methanol (MeOH, 20 vol %) and lactic acid (10 vol%) as sacrificial agents, respectively. Before photocatalytic reaction, the reactor was purged with Ar for 15 min to eliminate O_2. The evolved H_2 was analyzed on a gas chromatograph (thermal conductivity detector, TDX-01 column, Ar as carrier gas) per 1 h. The details for the measurement of apparent quantum yield (AQY) were declared in the Supplementary Material.

For the photocatalytic O_2 production, photocatalysts (10 mg) was well dispersed in an aqueous solution (80 mL) containing $AgNO_3$ (0.01 M) as an electron acceptor and La_2O_3 (0.16 g) as a pH buffer agent. Before photocatalytic reaction, the reactor was purged with Ar for 30 min to eliminate O_2. The evolved O_2 was analyzed on a gas chromatograph (thermal conductivity detector, TDX-01 column, Ar as carrier gas) per 1 h.

2.3. Computational method

The DFT calculations were accomplished by the Vienna ab-initio Simulation Package (VASP) codes. The core electrons were described by projected augmented wave (PAW) pseudo-potentials. The exchange and correlation effects of valence electrons were treated by the generalized gradient approximation (GGA) using the functional developed by Perdew-Burke-Ernzerhof (PBE). The g-C_3N_4 and N defects modified g-C_3N_4 were fully relaxed by the method of a conjugate-gradient algorithm with the criterion of force convergence in 0.02 eV $Å^{-1}$ and total energy convergence within 10^{-5} eV. The basis sets of plane waves were cut-off by 500 eV, and k-points mesh of g-C_3N_4 and N-defects modified g-C_3N_4 were generated by the Gamma center method ($3 \times 6 \times 2$) for structure relaxation. As for the band structure computation, due to the ripple of the N defects modified g-C_3N_4, the k path was changed from Γ-X-S-Y-Γ of the g-C_3N_4 to Γ-X-H_1-C-H-Y-Γ of the N defects modified g-C_3N_4 [21,26].

3. Results and discussion

3.1. Structure and chemical states for GCNs

The chemical structures of all the samples were analyzed by XRD and FTIR measurements to verify the formation of GCNs. Fig. 2a, b and S3 show the XRD patterns of all the GCNs samples. Basically, all the samples showed two typical diffraction peaks: a minor angle diffraction peak corresponded to in-plane repeating units of the continuous heptazine (tri-s-triazine) framework, and another relatively strong peak corresponded to the inter-layer stacking of conjugated aromatic systems, which were indexed to the (100) and (002) peaks of g-C_3N_4, respectively [39–41].

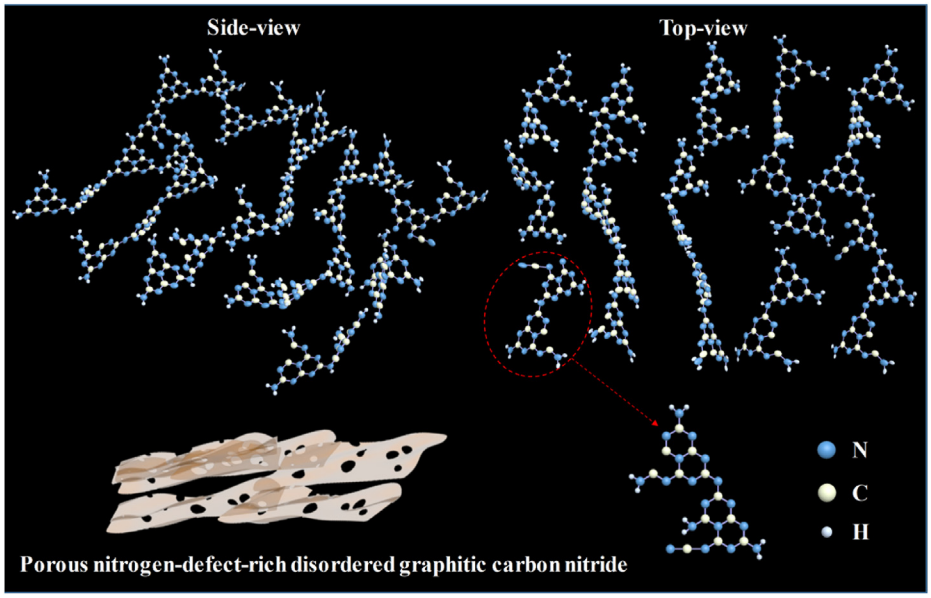

Fig. 1. Schematic illustration about the formation of porous nitrogen-defect-rich disordered graphitic carbon nitride. (A colour version of this figure can be viewed online.)

Meaningfully, it deserved special attention that the XRD pattern of BCN was obviously different from those of the other samples. Firstly, the (100) peak almost disappeared in the BCN pattern, indicating the long-range disordered structures in atomic arrangements [37]. Furthermore, the (100) peak of BCN appeared at a lower angle (12.64°) compared to those of the others, implying the in-plane repeating units structure of the continuous heptazine framework might be broken instead of numerous defects embedded into the in-planes of BCN [42]. Secondly, the (002) peak was extremely broad and weak, suggesting the periodic stacking of the layers along the c-axis for BCN was incompact and disorderly [43]. In addition, the (002) peak of BCN also located at a lower angle (26.71°) compared to those of the other GCNs samples, indicating a large interplanar distance of layered structure based on Bragg's Law. The XRD results confirmed that BCN had disordered g-C_3N_4 structure.

Table S1 shows the elemental compositions for the as-prepared GCNs samples from EA. Notably, BCN presented the largest atomic ratio of carbon to nitrogen element (the actual atomic ratio of carbon to nitrogen in g-C_3N_4 is commonly smaller than 0.75 in stoichiometry because of incomplete condensation of NH/NH_2 groups [6,40]), proving that nitrogen vacancies could be embedded in the structure of BCN. For the FTIR spectra, as shown in Fig. 2c, all the samples commonly showed spectra with typical characteristic peaks of g-C_3N_4: the peaks located at 2900–3300, 900–1700 and 810 cm^{-1} were assigned to the stretching vibrational absorptions of N–H bonds, aromatic C–N heterocycles and the out-of-plane bending vibrations of tri-striazine subunits, respectively [44]. Take the analysis and comparisons for all the as-prepared GCNs samples, the FTIR spectrum of BCN was a bit different from those of the others. The intensity of the N–H stretching peaks for BCN was progressive weak as compared with those of other samples, suggesting the low concentration of N–H groups in the structure [42]. Moreover, a peak at 2178 cm^{-1} was observed in the spectrum, which was assigned to the asymmetric stretching vibration of cyano groups (–C≡N) [45]. Note that the intensities of peaks (located between 900 and 1200 cm^{-1}) assigned to the stretching modes of aromatic C–N heterocycles in the "melon" framework for BCN was progressive strong as compared with those for other samples [43,45], indicating the polymerization degree of "melon" in BCN framework was higher than those in other sample. As a result, high polymerization degree would contribute to extended π-system, low proton concentration and enhanced transportation of charge carriers, thus making for high-efficiency photocatalytic performance. Fig. 2d shows closer investigation over the FTIR spectra (1700–1200 and 950–750 cm^{-1}) of all the as-prepared GCNs samples, it can be observed that two peaks attributed to bridging C–NH–C units of melon for BCN were different from the others and located at relatively higher wavenumber (1252 and 1422 cm^{-1}). Meanwhile, it presents that the peak belonging to the out-of-plane bending vibrations of tri-s-triazine subunits for BCN also appeared at a relatively higher wavenumber (812 cm^{-1}). These above differences indicated that BCN contained cyano group and nitrogen vacancies, resulting in significant changes in the constructions of aromatic C–N heterocycles and tri-s-triazine structure [27].

The surface chemical states for the as-prepared GCNs samples were next analyzed by XPS measurements. Fig. S4a shows the C 1s spectrum of BCN, three typical peaks centered at around 284.8, 286.0 and 288.2 eV could be indexed to the graphitic carbon C=C, sp^2-hybridized C connected to –NH and $-NH_2$ (C–NH and C–NH_2), and sp^2 C bonded to N in aromatic ring N–C=N, respectively [46–48]. For the N 1s spectrum of BCN (Fig. S4b), the four peaks located at 398.5, 399.6, 401.2, and 403.9 eV could be indexed to the sp^2-hybridized nitrogen in C–N=C (N_{2C}), tertiary nitrogen in N–$(C)_3$ (N_{3C}) groups, positive charge localization in heterocycles N–H, and π-excitation, respectively [46–48]. N_{2C} and N_{3C}, together with sp^2 C in N–C=N constitute the heptazine heterocyclic ring (C_6N_7) unit, constructing the basic substructure unit of the g-C_3N_4 polymers. In addition, systematic comparisons were made for the C 1s and N 1s spectra of all the GCNs samples, as shown in Fig. 3a and b, Table S2 and Table S3. Above all, on one hand, BCN showed the pretty large peak-area ratio for C species of C–NH&C–NH_2 to N–C=N, concluding a low content of C 2p orbital (sp^2 hybridized N–C=N), which generally indicated the reduction of crystallinity or much structural disorder in BCN [7]. On the other hand, there was a very small peak-area ratio for N species of C–N=C to N–$(C)_3$, it implied that the two-coordinated N atom in C–N=C was preferentially missing in the formation of BCN. Because the nitrogen vacancies and cyano group have been confirmed to embedding into

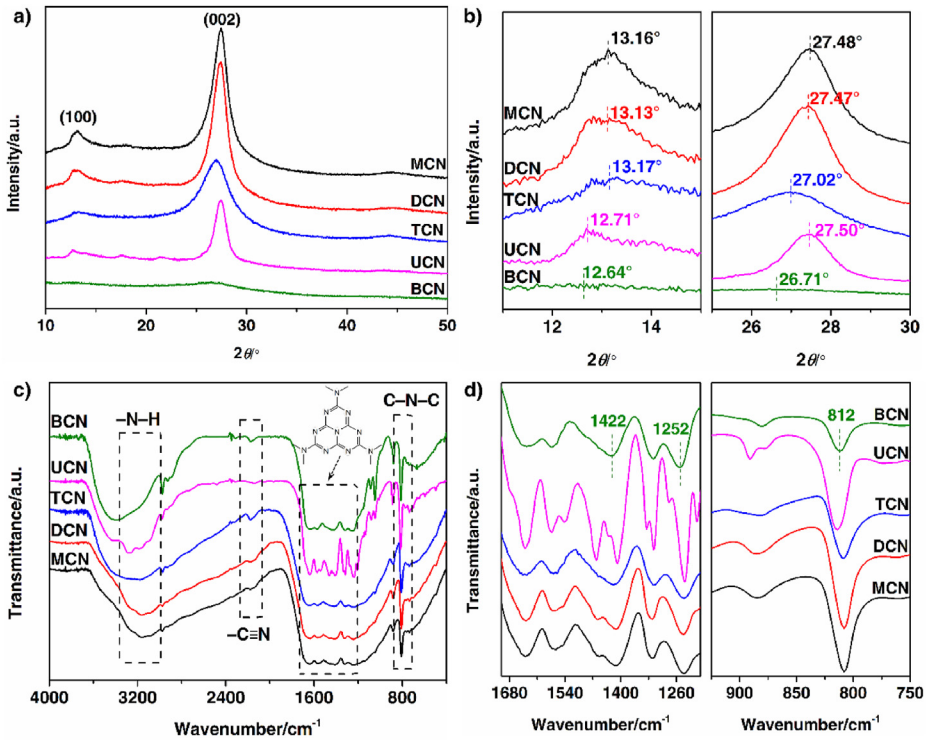

Fig. 2. (a) XRD patterns and (b) corresponding magnified results about the (100) (left) and (002) (right) diffraction peaks for MCN, DCN, TCN, UCN and BCN. (c) FTIR spectra and (d) corresponding magnified results in the ranges of 1700–1200 cm^{-1} (left) and 950–750 cm^{-1} (right) for MCN, DCN, TCN, UCN and BCN. (A colour version of this figure can be viewed online.)

the in-planes of BCN, it thus provided a clear evidence that the heptazine units in the BCN could be opened, resulting in providing much unsaturated N sites as well as offering much more active atoms for the functionalization of BCN. It is known that the residual amine groups (−NH&NH_2) containing N–H were responsible for the formation of hydrogen bonds in the GCN layer structure, which not only influenced the agglomeration of layers structure in bulk GCN but also functioned for maintaining the intralayer long-range atomic order for GCN [7,37]. BCN had the much small peak-area ratio for N species of N–H to N–$(C)_3$, consequently, the lack of the intralayer hydrogen bonds would lead to long-range disordered layer structure into small carbon nitride pieces of BCN. The structure fluctuation of the hydrogen bonding-free layers and weak van der Waals force between layers could perturb the periodic stacking and prevent the re-stacking of the BCN pieces, simultaneously [49,50]. The results were consistent with the XRD conclusions of the reason for weak and broad (100) and (002) peaks. Interestingly, BCN exhibited the minimum peak-area content for N species of π-excitation, which could be attributed to that the disorganized long-range structure constructed positive π-conjugated electronic system containing much reduced π-π interaction [8].

Synchrotron-based X-ray absorption near-edge structure (XANES) spectroscopy was also carried out to further expound the nitrogen-defect-rich disordered structure of BCN for the view of electronic structure evolution. As show in Fig. 3c, the C K-edge XANES spectra of all the as-prepared GCNs samples showed two peaks for illustrating the inplane and/or out-of plane C–N bonding, which could reveal the C–N hybridization and the possible charge transfer in GCN interlayers. In details, peak C1 was assigned to the carbon defects structures in GCN frameworks, and BCN had the weakest peak intensity to demonstrate the fewest amount of carbon defects [51,52], which was correlated to the EA results. Peak C2 was assigned to the N–C=N sp^2 hybridized states in which electron translated from the C 1s to 2p π* orbital [51,52]. In general, weaker intensity of peak C2 implies more structural disorder in GCN framework [53]. It observed that BCN had the weakest intensity of peak C2 as compared to those of the others, strongly suggesting the disordered structure of BCN. With regard to the N K-edge XANES spectra (Fig. 3d), all the samples showed two species of N sites in GCNs frameworks, i.e., the N1 site of C=N–C coordination structure in the heptazine units and the N2 site of N–$(C)_3$ bridging structure connecting with three heptazine units [51,54]. The N1 and N2 peaks of BCN both exhibited the weakest intensities compared with those of the others, indicating the existences of electron back-donation effect as well as nitrogen vacancies in BCN framework [51]. Especially, the peak intensity ratio of N1/N2 for BCN had the smallest value in all the as-prepared GCNs samples (Table S4), implying that there were many more nitrogen vacancies at N1 sites in BCN structure.

3.2. Micro-nano structure and textual properties for GCNs

The surface areas and porosities of all the as-prepared GCNs were characterized subsequently. Fig. 4a shows the nitrogen absorption-desorption isotherms for all the samples. Different from the others, BCN and UCN presented high adsorption capacities in high relative pressure ($P/P_0 > 0.8$), demonstrating the existence of abundant mesopores and macropores in BCN and UCN. As shown in Table 1, BCN had a large surface area (45.3 $m^2\ g^{-1}$) close to that of UCN. Moreover, BCN showed the largest pore volume (0.283 $cm^3\ g^{-1}$) but relatively small pore size (11.2 nm), implying the existence of a vast amount of pores in BCN. According to the pore-size distribution curves of all the as-prepared GCNs samples (Fig. S5), BCN possessed similar pore-size distribution to that of UCN, and the mainly distribution range was 1–54 nm, particularly smaller than 1.8 nm. It was thus deduced that BCN not only had a

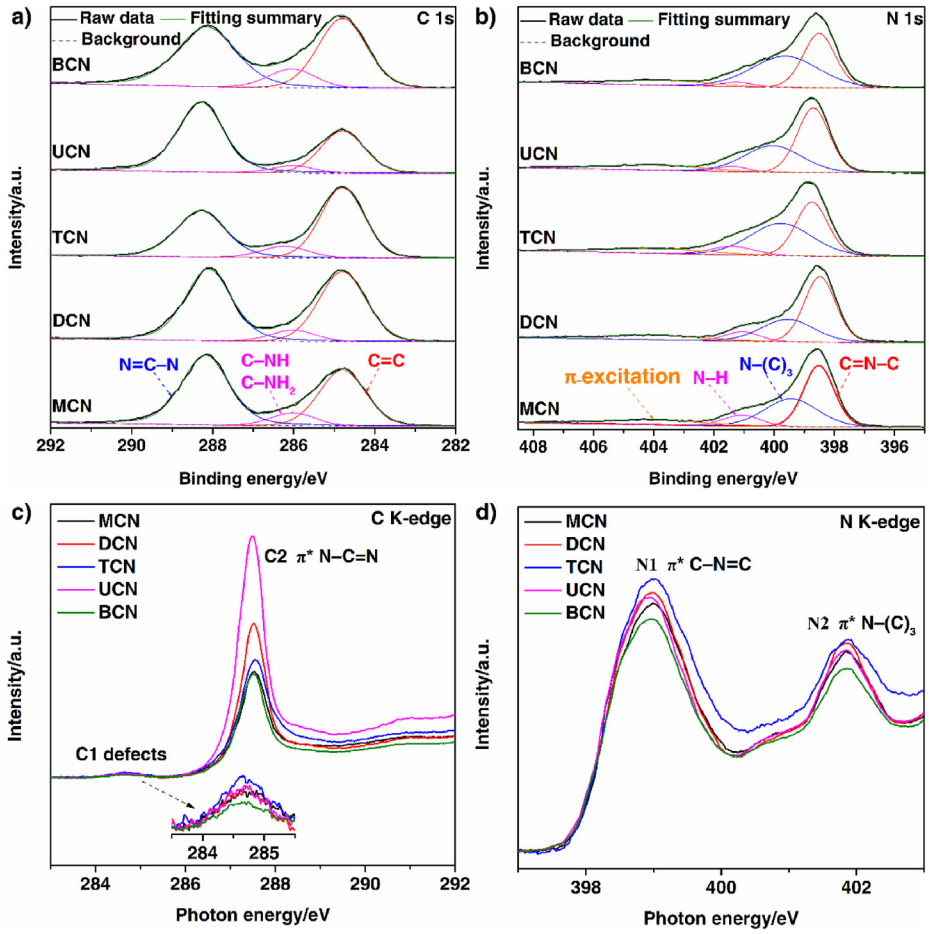

Fig. 3. High-resolution XPS spectra of (a) C 1s and (b) N 1s for BCN, UCN, TCN, DCN and MCN. (c) C K-edge XANES and (d) N K-edge XANES spectra for BCN, UCN, TCN, DCN and MCN. (A colour version of this figure can be viewed online.)

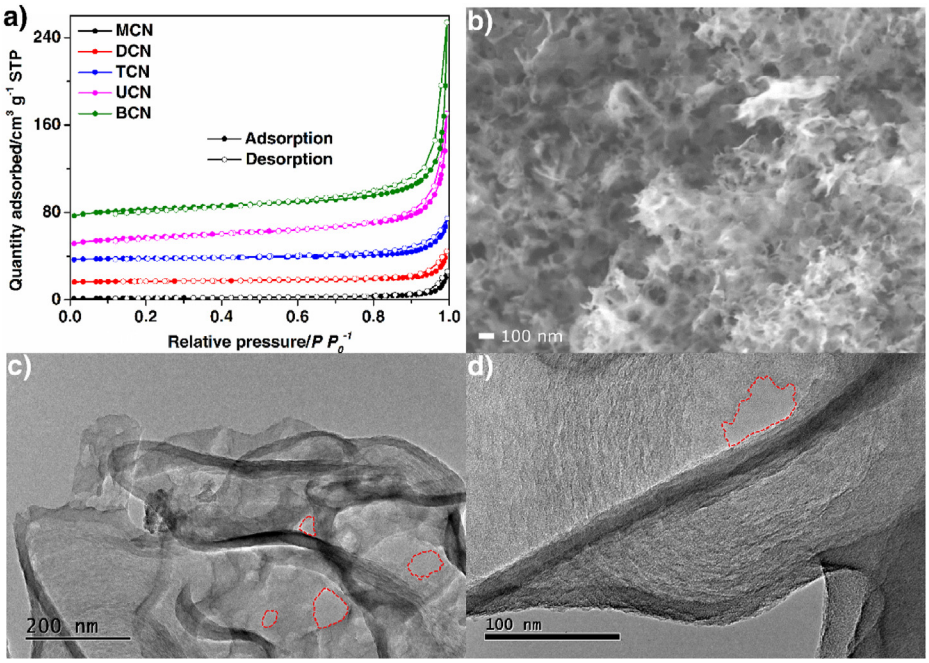

Fig. 4. (a) N_2 adsorption–desorption isotherms for MCN, DCN, TCN, UCN and BCN. (b) SEM and (c, d) TEM images for BCN, red circles in (c, d) demonstrated in-plane holes. The isotherms in (a) were shifted upward by 0, 15, 35, 45, and 65 $cm^3\ g^{-1}$ STP, respectively. (A colour version of this figure can be viewed online.)

Table 1
Textual properties, bandgaps, average decay lifetimes, H_2-production rates and O_2-production rates of BCN, UCN, TCN, DCN and MCN samples.

Sample	Surface area/m^2 g^{-1}	Pore volume/cm^3 g^{-1}	Pore size/nm	Band gap/eV	Average decay lifetime/ns	H_2-production rate/μmol h^{-1} g_{cat}^{-1}	O_2-production rate/μmol h^{-1} g_{cat}^{-1}
BCN	45.3	0.283	11.2	2.45	5.01	7026	251
UCN	43.6	0.194	80.7	2.75	6.13	3120	162
TCN	10.3	0.061	9.0	2.55	5.78	1242	151
DCN	7.2	0.046	11.5	2.67	8.13	849	300
MCN	5.7	0.040	12.1	2.63	6.61	680	96

large amount of mesopores and macropores, but also numerous micropores. The morphologies and microstructures for the as-prepared GCNs were investigated by SEM and TEM, and the related results are presented in Fig. 4b–d, S6 and S7. As observing from the SEM images (Fig. 4b, S6a and b), BCN possessed chipping-like structure with loose and curly morphology without aggregation. In addition, the low-magnification TEM image (Fig. S7a) revealed that the micro-nano morphology of BCN was quite similar to that of graphene. Fig. 4c and d further showed that BCN appeared as twisted ultrathin layers with edges rolling up, and looked like dancing ribbons. It was demonstrated that there existed many in-plane holes with the sizes from several to dozens of nanometers in the ultrathin layers, indicating the porous layered structure of BCN.

3.3. Optical and EPR properties for GCNs

Usually, the structural distortion and nitrogen defects could greatly extend the optical properties of GCNs [18,50]. As shown in Fig. 5a, the optical properties of all the as-prepared GCNs samples were studied by UV–vis spectra. BCN was enabled to possess the best light absorption ability compared with the others, and its absorption edge was at about 525 nm. Moreover, BCN exhibited remarkable light absorption tails in the long wavelengths range (500–800 nm), mainly owing to the presence of abundant nitrogen vacancies [54]. In addition, inset in Fig. 5a shows digital photographs of samples with a mass of 100 mg in each bottle. BCN appeared fluffy with a color of brown gray, which could be corresponding to the large surface area and porous structure of BCN, as well as its good optical property. As for the EPR spectra (Fig. 5d), all the as-prepared GCNs had a single Lorentzian line with the g value of 2.0028, which was ascribed to unpaired electrons of sp^2 C atoms in the π-conjugated aromatic rings [45,55]. Compared with those for UCN, TCN, DCN and MCN, the stronger EPR signal for BCN indicated the higher concentration of lone electron pairs, suggesting the defect structure in BCN with more unsaturated N sites [27,45]. Meanwhile, the bandgap energies of all the as-prepared GCNs samples were derived by the Kubelka–Munk method, as shown in Fig. S8. BCN showed a narrow bandgap of 2.45 eV, and the bandgaps of MCN, DCN, TCN and UCN were calculated to be 2.63,

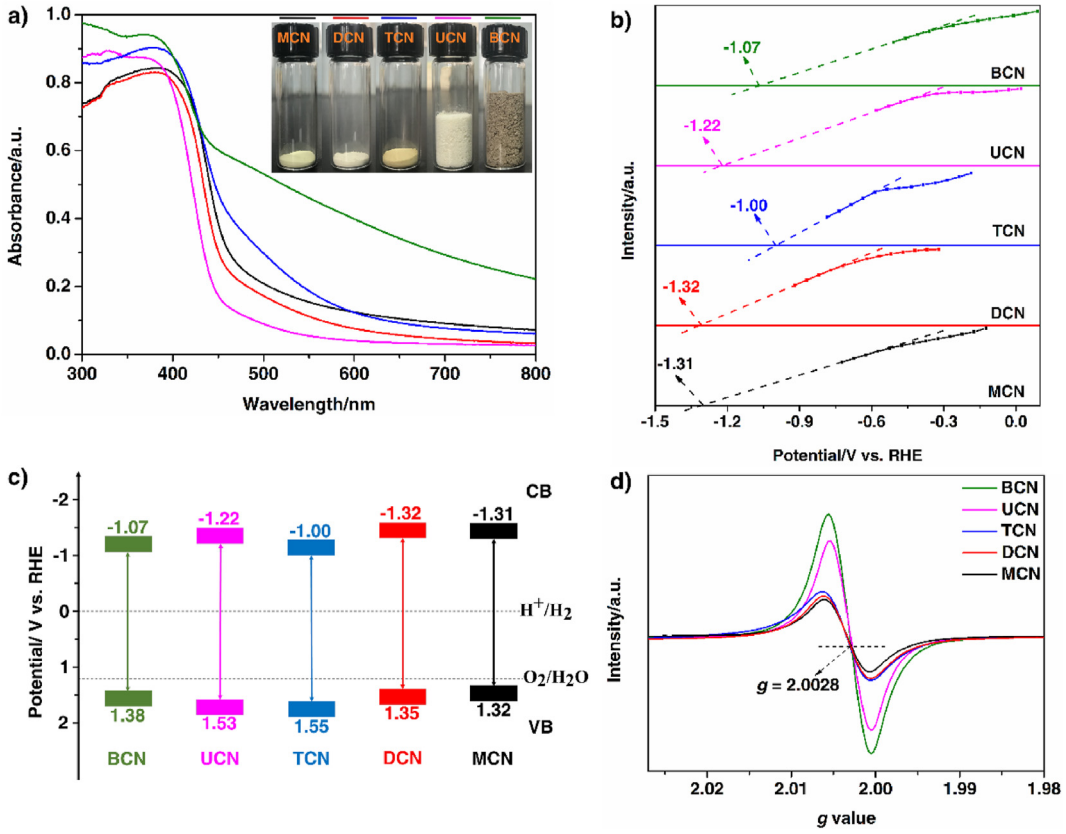

Fig. 5. (a) UV–vis spectra, (b) Mott-Schottky plots, (c) eletronic band structure alignments and (d) EPR spectra for MCN, DCN, TCN, UCN and BCN. Inset in (a) shows a digital photograph of samples with the mass is 100 mg, respectively. (A colour version of this figure can be viewed online.)

2.67, 2.55 and 2.75 eV, respectively. Based on the analysis about the valence band maximum (VBM) values by valence band (VB) XPS spectra (Fig. S9) and the conduction band minimum (CBM) values by Mott-Schottky (MS) plots (Fig. 5b), the band-structure alignments for all the as-prepared GCNs samples are schematically given in Fig. 5c. For BCN, the CBM and VBM position were at about −1.07 V and 1.38 V vs. RHE, respectively, indicating that BCN satisfied the thermodynamic requirements for the redox reactions of water splitting, i.e., H_2 and O_2 production.

3.4. DFT calculations of band structure for BCN

For BCN, as a semiconductor with long-range disordered structures in atomic arrangements and broken in-plane repeating heptazine framework units, its small energy level difference between the highest occupied and lowest unoccupied electronic states could make for a small bandgap. In addition, the coexistence of cyano groups and N vacancies in the heptazine unit cell of BCN would usually produce a defect energy level consisted of both C 2p and N 2p orbitals above the VBM, which coincided with the strong absorption tail observed in BCN sample. The defect structure could also make a contribution to the narrow bandgap of BCN. Density-functional theory (DFT) calculations were carried out to further reveal the electronic structure of g-C_3N_4 as induced by nitrogen defects (−C≡N group and N vacancy) and disordered structure. Structure models of g-C_3N_4 without and with N defects were built to simulate the structural characteristics of pristine g-C_3N_4 and BCN, respectively (Fig. 6a, b, d and e). The calculation results showed that, after the introduction of nitrogen defects into the unit cell of g-C_3N_4, the structure of g-C_3N_4 became disordered and the bandgap energy decreased from 2.36 to 2.20 eV (Fig. 6c and f), which agreed well with the structure of BCN and the general trend in the bandgap data above. Moreover, the CB of g-C_3N_4 without N defects consisted of both C 2p and N 2p orbitals, while the VB was mainly composed of N 2p orbitals (edge N atoms of heptazine units), consistent with previously reported results [56]. Furthermore, for g-C_3N_4 with N defects, a defect energy level composed of both C 2p and N 2p orbitals appeared above the VB position, which was reflected by the remarkable absorption tail observed in the nitrogen-defect-rich disordered g-C_3N_4 (BCN).

3.5. Photoexcitation processes and photo-generated charge carriers dynamics for GCNs

To reveal the photoexcitation process of the photocatalyst, the C K-edge and N K-edge XANES spectra for all the as-prepared GCNs were both measured in the dark and under illumination to explore the photo-excited electron transition from the lone pair states (i.e., occupied states) to the π* states (i.e., unoccupied states). For both C and N K-edge XANES spectra (Fig. 7a and b), all the as-prepared GCNs showed higher intensities under light irradiation than those under dark conditions, and the irradiation−dark intensity variations for BCN were generally more obvious than those of the others. Especially, the irradiation−dark intensity variation of C K-edge XANES spectra for BCN was notably obvious as compared to those of the other GCNs, which indicated plenty of empty states were generated in the CB of BCN [51,52]. The differences in C and N K-edge XANES spectra between BCN and the others meant that the more efficient electron excitation from the occupied orbitals in the VB to the unoccupied states in the CB was occurred in the BCN structure [51,53]. It also could be evolved that the nitrogen defects and disordered structure in BCN framework provided more unsaturated sites to facilitate the formation of unpaired electrons and benefit the photo-induced generation of charge carriers for photocatalytic reaction. Furthermore, the possibility of recombination for photo-generated charge carriers was then explored by photoluminescence measurements. Fig. 7c shows the steady-state PL spectra of MCN, DCN, TCN, UCN and BCN samples. BCN had the weakest steady-state PL intensity, indicating the effective suppression about the recombination of photo-generated charge carriers [57–59]. This improvement could be attributed to two aspects: on one hand, the large interlayer distance and fragmented

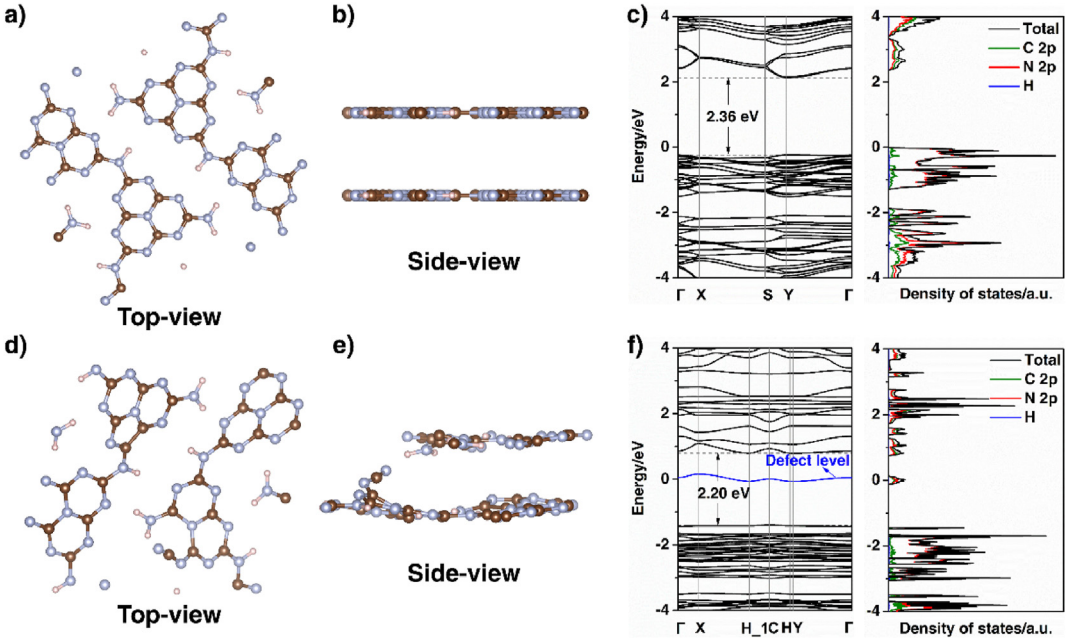

Fig. 6. (a, b, d and e) Structure models for g-C_3N_4 (a, b) without N defects and (d, e) with N defects (including −C≡N group and N vacancy). (c, f) Calculated band structures and corresponding density of states (DOS) for g-C_3N_4 (c) without and (f) with N defects, respectively. (A colour version of this figure can be viewed online.)

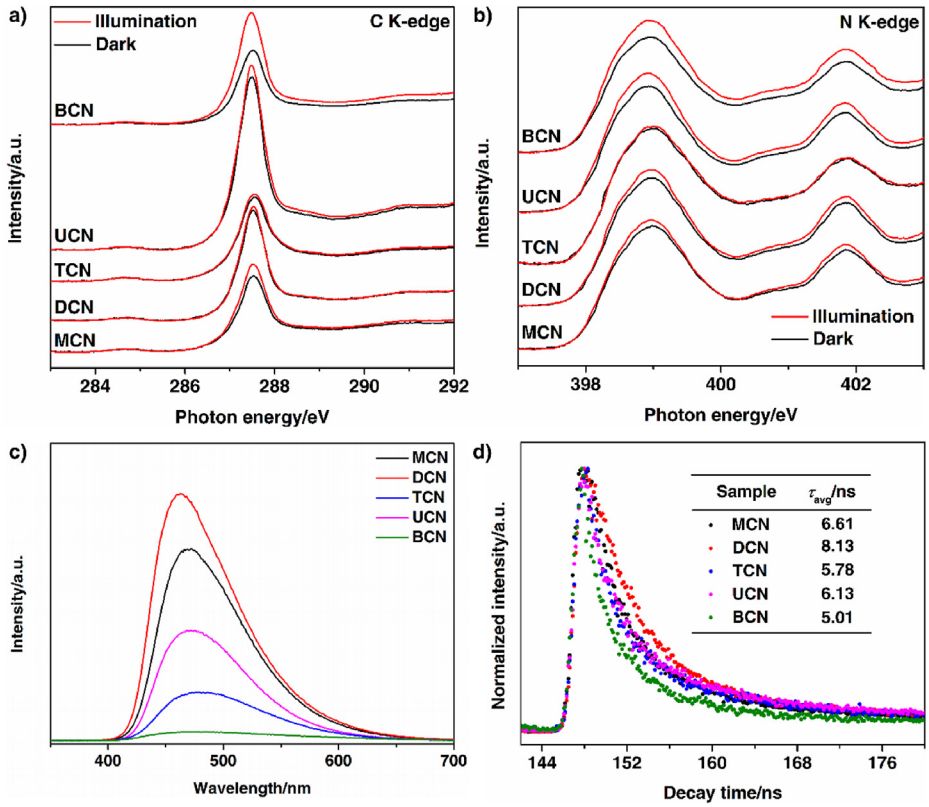

Fig. 7. (a) C K-edge and (b) N K-edge XANES spectra with or without illumination for BCN, UCN, TCN, DCN and MCN. (c) PL spectra and (d) time-resolved transient PL decay spectra for MCN, DCN, TCN, UCN and BCN at room temperature. (A colour version of this figure can be viewed online.)

porous structure of BCN resulted in short migration distances for photo-generated charge carriers [50]; on the other hand, the cyano terminal (−C≡N) groups located at the sheet edges of BCN acted as electron acceptors to promote the migration of photo-generated charge carriers [45,57]. Moreover, the transfer dynamics of charge carriers were further investigated by measuring transient PL decay spectra, the results are shown in Fig. 7d. The order of average lifetimes for all the as-prepared GCNs samples was demonstrated as BCN < TCN < UCN < MCN < DCN, which was consistent with the order of steady-state PL intensity. The results implied that BCN could own additional nonradiative decay channels to promote the electron transfer due to the nitrogen-defect-rich disordered g-C_3N_4 networks, leading to effective suppression of the electron−hole recombination [60−64].

3.6. Photocatalytic performance for GCNs

Photocatalytic H_2 evolution and O_2 evolution were measured to examine the photocatalytic performances of all the as-prepared GCNs samples. Fig. S10 presents the photocatalytic H_2-evolution activities for BCN with using different sacrificial agents. BCN showed the highest photocatalytic H_2-evolution activity with using formic acid as sacrificial reagent. However, formic acid can decompose itself to produce hydrogen with light irradiation and stirring, we preferred TEOA as sacrificial reagent to evaluate the photocatalytic H_2-evolution performance for the photocatalyst. Fig. 8a presents the photocatalytic H_2-evolution rate for all the samples under visible-light irradiation with using TEOA as sacrificial agent. Compared with other GCNs samples, BCN behaved the highest photocatalytic activity for H_2 evolution (7026 μmol h^{-1} g_{cat}^{-1}) under the same measurement condition. In addition, the photocatalytic H_2-evolution activity of BCN was further enhanced to an ultrahigh value (19583 μmol h^{-1} g_{cat}^{-1}) by optimizing the addition amount of K_2HPO_4 into the photocatalytic reaction solution (Fig. S11). K_2HPO_4 was employed to mimic phosphate-involving natural photosynthesis environment, in which the light-dependent reactions occur in thylakoid membranes featuring phosphates that promote migration of electrons and reduction of protons [65]. In order to intuitively demonstrate the photocatalytic H_2-evolution activity of BCN, photocatalytic H_2-evolution reaction was performed in an unsealed breaker. As shown in Supplementary Video and Fig. S12, a large amount of bubbles were generated and detached out from the surface of photocatalyst under visible-light irradiation. Fig. 8b and Fig. S13 present the AQYs of BCN for H_2 evolution at different wavelengths, and the AQY was estimated to be 45.5% at 420 nm, which is one of the highest values for GCNs photocatalysts (Table S6). The AQY values at different wavelengths showed good consistence with the optical absorption of BCN, revealing that the photocatalytic H_2-evolution reaction was primarily driven by the photocatalytic process of photo-excitation of BCN [55,66]. In addition, cyclic test of photocatalytic activity for H_2 evolution was performed to check the photocatalytic stability of BCN, as shown in Fig. 8c. The photocatalytic H_2-evolution activity for BCN showed no decay in five cyclic tests for 15 h, indicating the good photocatalytic stability of BCN. Furthermore, as shown in Fig. S15, XRD, FTIR and XPS measurements were employed to characterize the recovered photocatalyst (BCN−R) after photocatalytic H_2-evolution reaction. It almost had no difference between BCN−R and BCN, further indicating the good stability of BCN for photocatalytic H_2 evolution. Additionally, other GCN (BCN−520

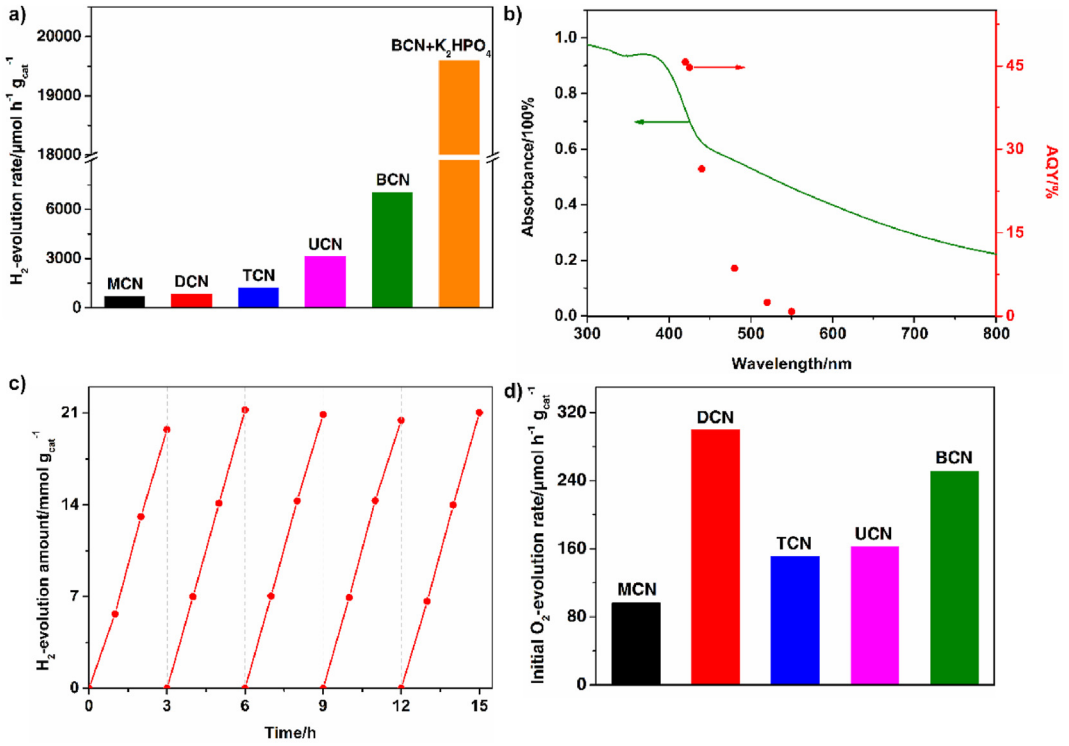

Fig. 8. (a) Photocatalytic H_2-evolution activities for MCN, DCN, TCN, UCN, BCN and BCN + K_2HPO_4 under visible-light irradiation ($\lambda > 420$ nm). (b) Wavelength-determined AQYs for BCN + K_2HPO_4. (c) Photocatalytic H_2-evolution stability test of BCN under visible-light irradiation ($\lambda > 420$ nm). (d) Photocatalytic O_2-evolution activities for MCN, DCN, TCN, UCN and BCN under visible-light irradiation ($\lambda > 420$ nm). "BCN + K_2HPO_4" represented the photocatalytic H_2-evolution activities for BCN by adding 0.08 mol of K_2HPO_4 in the reaction solution while keeping other measurement conditions the same. The above photocatalytic H_2-evolution reactions were performed by using TEOA as the sacrificial agent. (A colour version of this figure can be viewed online.)

and BCN−600) obtained by calcining biuret at other high temperature were characterized and evaluated by photocatalytic H_2 evolution, as shown in Fig. S16. XRD and FTIR results showed BCN−520, BCN and BCN−600 had the typical structural characteristics of g-C_3N_4. With increasing the preparation temperature, the biuret-derived g-C_3N_4 became more disordered, and had more N defects (Fig. S16a). UV−vis spectra showed BCN−520, BCN and BCN−600 presented similar light absorption ability, absorption edge was gradually and slightly red shift with increasing the preparation temperature (Fig. S16c). The photocatalytic test showed BCN had the highest H_2-evolution activity (Fig. S16d). In addition to photocatalytic H_2 evolution, photocatalytic O_2 evolution was examined in the presence of $AgNO_3$ as sacrificial agent in photocatalytic reaction solution. As shown in Fig. 8d and S17, BCN could enable water oxidation with an initial rate of 251 μmol h^{-1} g_{cat}^{-1} under visible-light irradiation. Considering the photocatalytic overall water splitting of BCN in pure water, neither H_2 nor O_2 was detected when the photocatalytic reaction was carried out without employing any sacrificial reagent.

According to all of the above characterizations and analysis, the immanent mechanism of ultrahigh photocatalytic H_2-production activity for BCN could be mainly attributed to the following aspects: Firstly, the nitrogen-defect-rich disordered structure made BCN possess smaller bandgap than the commonly available GCNs. BCN had a wide light-absorption range and thus utilized a large portion of solar radiation. Secondly, the recombination of photo-generated electron-holes for BCN was effectively inhibited, due to the large interlayer distance and fragmented porous structure, as well as the existence of cyano terminal (−C≡N) groups located at the sheet edges of BCN. Finally, BCN had abundant reactive sites for photocatalytic reaction because of its large specific surface area and numerous N defects. The synergistic effect of above advantages provided strong support for BCN to realize ultrahighly efficient activity for photocatalytic H_2 evolution.

4. Conclusions

Biuret was employed as a new precursor to prepare disordered nitrogen-defect-rich porous graphitic carbon nitride (BCN) by the thermal polymerization method, and for systematic comparisons, other conventional precursors (melamine, dicyandiamide, thiourea and urea) were also employed to prepare commonly available GCNs (MCN, DCN, TCN and UCN) under the identical conditions. The resultant biuret-derived BCN possessed unique crystal and textural structures. On the one hand, numerous N defects and long-range atomic disordered structure in BCN led to extended visible-light absorption, improved separation of photo-generated charge carriers, and rich available reactive sites, cyano terminal (−C≡N) groups located at the sheet edges of BCN acted as electron acceptors to promote the migration of photo-generated charge carriers. On the other hand, large surface area and vast amounts of pores in BCN also generated many reactive sites. As a result, BCN behaved ultrahighly efficient activity for photocatalytic H_2 evolution and also excellent activity for photocatalytic O_2 evolution, the AQY for photocatalytic H_2 production was estimated to be 45.5% at 420 nm, which is one of the highest values for GCN photocatalysts. Biuret could be the optimal choice for the preparation of high-performance GCN according to the reports so far. This study presented a promising strategy to prepare high-efficiency carbon nitrides, and provided insight into the structural design of carbon

nitrides for application of more efficient solar energy conversion.

CRediT authorship contribution statement

Cheng Cheng: Conceptualization, Methodology, Validation, Writing – original draft, Investigation. **Jinwen Shi:** Writing – review & editing, Supervision, Project administration, Resources, Funding acquisition. **Linyuan Wen:** Methodology, Formal analysis. **Chung-Li Dong:** Methodology, Formal analysis. **Yu-Cheng Huang:** Methodology, Formal analysis. **Yazhou Zhang:** Writing – review & editing. **Shichao Zong:** Writing – review & editing. **Zhidan Diao:** Writing – review & editing. **Shaohua Shen:** Writing – review & editing. **Liejin Guo:** Supervision, Project administration, Resources, Funding acquisition.

Declaration of competing interest

The authors declare that they have no known competing financial interests or personal relationships that could have appeared to influence the work reported in this paper.

Acknowledgements

This work is supported by the Basic Science Center Program for Ordered Energy Conversion of the National Natural Science Foundation of China (No. 51888103), the National Natural Science Foundation of China (No. 51961165103), and the National Key Research and Development Project (No. 2018YFB1502000). We thank the Instrument Analysis Center of Xi'an Jiaotong University for their assistance with TEM analysis.

Appendix A. Supplementary data

Supplementary data to this article can be found online at https://doi.org/10.1016/j.carbon.2021.05.030.

References

[1] A. Kudo, Y. Miseki, Heterogeneous photocatalyst materials for water splitting, Chem. Soc. Rev. 38 (2009) 253–278.
[2] Q. Wang, K. Domen, Particulate photocatalysts for light-driven water splitting: mechanisms, challenges, and design strategies, Chem. Rev. 120 (2019) 919–985.
[3] W. Ding, J. Shi, W. Wei, C. Cao, H. Jin, A molecular dynamics simulation study on solubility behaviors of polycyclic aromatic hydrocarbons in supercritical water/hydrogen environment, Int. J. Hydrogen Energy 52 (2021) 28062–28069.
[4] S. Nishioka, T. Oshima, S. Hirai, D. Saito, K. Hojo, T.E. Mallouk, K. Maeda, Excited carrier dynamics in a dye-sensitized niobate nanosheet photocatalyst for visible-light hydrogen evolution, ACS Catal. 11 (2020) 659–669.
[5] H. Yan, J. Yang, G. Ma, G. Wu, X. Zong, Z. Lei, J. Shi, C. Li, Visible-light-driven hydrogen production with extremely high quantum efficiency on Pt-PdS/CdS photocatalyst, J. Catal. 266 (2009) 165–168.
[6] Y. Zheng, J. Liu, J. Liang, M. Jaroniec, S. Qiao, Graphitic carbon nitride materials: controllable synthesis and applications in fuel cells and photocatalysis, Energy Environ. Sci. 5 (2012) 6717–6731.
[7] Z. Zhou, Y. Zhang, Y. Shen, S. Liu, Y. Zhang, Molecular engineering of polymeric carbon nitride: advancing applications from photocatalysis to biosensing and more, Chem. Soc. Rev. 47 (2018) 2298–2321.
[8] W. Ong, L. Tan, Y. Ng, S. Yong, S. Chai, Graphitic carbon nitride ($g\text{-}C_3N_4$)-based photocatalysts for artificial photosynthesis and environmental remediation: are we a step closer to achieving sustainability? Chem. Rev. 116 (2016) 7159–7329.
[9] M. Rahman, K. Davey, C. Mullins, Tuning the intrinsic properties of carbon nitride for high quantum yield photocatalytic hydrogen production, Adv. Sci. 5 (2018) 1800820–1800833.
[10] J. Fu, J. Yu, C. Jiang, C. Cheng, $g\text{-}C_3N_4$-based heterostructured photocatalysts, Adv. Energy Mater. 8 (2018) 1701503–1701533.
[11] G. Zhang, Z. Lan, X. Wang, Conjugated polymers: catalysts for photocatalytic hydrogen evolution, Angew. Chem. Int. Ed. 55 (2016) 15712–15727.
[12] C. Cheng, L. Mao, J. Shi, F. Xue, S. Zong, B. Zheng, L. Guo, $NiCo_2O_4$ nanosheet as a novel oxygen-evolution-reaction cocatalyst in-situ bonded on $g\text{-}C_3N_4$ photocatalyst for excellent overall water splitting, J. Mater. Chem. https://doi.org/10.1039/D1TA00241D..
[13] G. Dong, K. Zhao, L. Zhang, Carbon self-doping induced high electronic conductivity and photoreactivity of $g\text{-}C_3N_4$, Chem. Commun. 48 (2012) 6178–6180.
[14] F. Guo, J. Chen, M. Zhang, B. Gao, B. Lin, Y. Chen, Deprotonation of $g\text{-}C_3N_4$ with Na ions for efficient nonsacrificial water splitting under visible light, J. Mater. Chem. A. 4 (2016) 10806–10809.
[15] S. Yan, Z. Li, Z. Zou, Photodegradation of Rhodamine B and methyl orange over boron-doped $g\text{-}C_3N_4$ under visible light irradiation, Langmuir 26 (2010) 3894–3901.
[16] J. Zhang, S. Gong, N. Mahmood, L. Pan, X. Zhang, J. Zou, Oxygen-doped nanoporous carbon nitride via water-based homogeneous supramolecular assembly for photocatalytic hydrogen evolution, Appl. Catal. B Environ. 221 (2018) 9–16.
[17] G. Zhang, M. Zhang, X. Ye, X. Qiu, S. Lin, X. Wang, Iodine modified carbon nitride semiconductors as visible light photocatalysts for hydrogen evolution, Adv. Mater. 26 (2014) 805–809.
[18] J. Ran, T. Ma, G. Gao, X. Du, S. Qiao, Porous P-doped graphitic carbon nitride nanosheets for synergistically enhanced visible-light photocatalytic H_2 production, Energy Environ. Sci. 8 (2015) 3708–3717.
[19] S. Guo, Z. Deng, M. Li, B. Jiang, C. Tian, Q. Pan, H. Fu, Phosphorus-doped carbon nitride tubes with a layered micro-nanostructure for enhanced visible-light photocatalytic hydrogen evolution, Angew. Chem. Int. Ed. 55 (2016) 1830–1834.
[20] X. Li, B. Wang, W. Yin, J. Di, J. Xia, W. Zhu, H. Li, Cu^{2+} modified $g\text{-}C_3N_4$ photocatalysts for visible light photocatalytic properties, Acta Phys. Chim. Sin. 236 (2020) 1902001.
[21] G.O. Hartley, N. Martsinovich, Computational design of graphitic carbon nitride photocatalysts for water splitting, Faraday Discuss 227 (2021) 341.
[22] J. Zhang, X. An, N. Lin, W. Wu, L. Wang, Z. Li, R. Wang, Y. Wang, J. Liu, M. Wu, Engineering monomer structure of carbon nitride for the effective and mild photooxidation reaction, Carbon 100 (2016) 450–455.
[23] Y. Chen, X. Wang, Template-free synthesis of hollow $G\text{-}C_3N_4$ polymer with vesicle structure for enhanced photocatalytic water splitting, J. Phys. Chem. C 122 (2018) 3786–3793.
[24] C. Liu, H. Huang, L. Ye, S. Yu, N. Tian, X. Du, T. Zhang, Y. Zhang, Intermediate-mediated strategy to horn-like hollow mesoporous ultrathin $g\text{-}C_3N_4$ tube with spatial anisotropic charge separation for superior photocatalytic H_2 evolution, Nanomater. Energy 41 (2017) 738–748.
[25] P. Niu, L. Yin, Y. Yang, G. Liu, H. Cheng, Increasing the visible light absorption of graphitic carbon nitride (melon) photocatalysts by homogeneous delf-modification with nitrogen vacancies, Adv. Mater. 26 (2014) 8046–8052.
[26] L. Lin, H. Ou, Zhang, Y. Zhang, X. Wang, Tri-s-triazine-based crystalline graphitic carbon nitrides for highly efficient hydrogen evolution photocatalysis, ACS Catal. 6 (2016) 3921–3931.
[27] Y. Zhang, S. Zong, C. Cheng, J. Shi, P. Guo, X. Guan, B. Luo, S. Shen, L. Guo, Rapid high-temperature treatment on graphitic carbon nitride for excellent photocatalytic H_2-evolution performance, Appl. Catal. B Environ. 233 (2018) 80–87.
[28] S. Yan, Z. Li, Z. Zou, Photodegradation performance of $g\text{-}C_3N_4$ fabricated by directly heating melamine, Langmuir 25 (2009) 10397–10401.
[29] H. Dong, X. Guo, C. Yang, Z. Ouyang, Synthesis of $g\text{-}C_3N_4$ by different precursors under burning explosion effect and its photocatalytic degradation for tylosin, Appl. Catal. B Environ. 230 (2018) 65–76.
[30] J. Zhang, M. Grzelczak, Y. Hou, K. Maeda, K. Domen, X. Fu, M. Antonietti, X. Wang, Photocatalytic oxidation of water by polymeric carbon nitride nanohybrids made of sustainable elements, Chem. Sci. 3 (2012) 443–446.
[31] J. Liu, T. Zhang, Z. Wang, G. Dawson, W. Chen, Simple pyrolysis of urea into graphitic carbon nitride with recyclable adsorption and photocatalytic activity, J. Mater. Chem. 21 (2011) 14398–14401.
[32] Z. Pan, Y. Zheng, F. Guo, P. Niu, X. Wang, Decorating CoP and Pt nanoparticles on graphitic carbon nitride nanosheets to promote overall water splitting by conjugated polymers, ChemSusChem 10 (2017) 87–90.
[33] S. Huang, J. Lang, C. Du, F. Bian, Y. Su, X. Wang, Enhanced driving force and charge separation efficiency in disordered $SnNb_xO_y$: boosting photocatalytic activity toward water reduction, Chem. Eng. J. 309 (2017) 313–320.
[34] Z. Chen, J. Xing, H. Jiang, H. Yang, Disordered $Co_{1.28}Mn_{1.71}O_4$ as a visible-light-responsive photocatalyst for hydrogen evolution, Chemistry 19 (2013) 4123–4127.
[35] V. Khabashesku, J. Zimmerman, J. Margrave, Powder synthesis and characterization of amorphous carbon nitride, Chem. Mater. 12 (2000) 3264–3270.
[36] J. Xu, M. Antonietti, The performance of nanoparticulate graphitic carbon nitride as an amphiphile, J. Am. Chem. Soc. 139 (2017) 6026–6029.
[37] Y. Kang, Y. Yang, L. Yin, X. Kang, G. Liu, H. Cheng, An amorphous carbon nitride photocatalyst with greatly extended visible-light-responsive range for photocatalytic hydrogen generation, Adv. Mater. 27 (2015) 4572–4577.
[38] Y. Zhang, J. Liu, G. Wu, W. Chen, Porous graphitic carbon nitride synthesized via direct polymerization of urea for efficient sunlight-driven photocatalytic hydrogen production, Nanoscale 4 (2012) 5300–5303.
[39] C. Cheng, J. Shi, F. Du, S. Zong, X. Guan, Y. Zhang, M. Liu, L. Guo, Simply blending Ni nanoparticles with typical photocatalysts for efficient photocatalytic H_2 production, Catal. Sci. Technol. 9 (2019) 7016–7022.
[40] X. Wang, K. Maeda, A. Thomas, K. Takanabe, G. Xin, J. Carlsson, K. Domen, M. Antonietti, A metal-free polymeric photocatalyst for hydrogen production from water under visible light, Nat. Mater. 8 (2009) 76–80.
[41] F. Fina, S. Callear, G. Carins, J. Irvine, Structural investigation of graphitic

carbon nitride via XRD and neutron diffraction, Chem. Mater. 27 (2015) 2612–2618.
[42] D. Zhang, Y. Guo, Z. Zhao, Porous defect-modified graphitic carbon nitride via a facile one-step approach with significantly enhanced photocatalytic hydrogen evolution under visible light irradiation, Appl. Catal. B Environ. 226 (2018) 1–9.
[43] H. Yu, R. Shi, Y. Zhao, T. Bian, Y. Zhao, C. Zhou, G. Waterhouse, L. Wu, C. Tung, T. Zhang, Alkali-assisted synthesis of nitrogen deficient graphitic carbon nitride with tunable band dtructures for efficient visible-light-driven hydrogen evolution, Adv. Mater. 29 (2017) 1605148–1605154.
[44] F. Xue, M. Liu, C. Cheng, J. Deng, S. Shi, Localized NiS_2 quantum dots on g-C_3N_4 nanosheets for efficient photocatalytic hydrogen production from water, ChemCatChem 10 (2018) 5441–5448.
[45] G. Liu, G. Zhao, W. Zhou, Y. Liu, H. Pang, H. Zhang, D. Hao, X. Meng, P. Li, T. Kako, J. Ye, In situ bond modulation of graphitic carbon nitride to construct p-n homojunctions for enhanced photocatalytic hydrogen production, Adv. Funct. Mater. 26 (2016) 6822–6829.
[46] T. Song, P. Zhang, T. Wang, A. Ali, H. Zeng, Alkali-assisted fabrication of holey carbon nitride nanosheet with tunable conjugated system for efficient visible-light-driven water splitting, Appl. Catal. B Environ. 224 (2018) 877–885.
[47] X. Fang, R. Gao, Y. Yang, D. Yan, A cocrystal precursor strategy for carbon-rich graphitic carbon nitride toward high-efficiency photocatalytic overall water Splitting, iScience 16 (2019) 22–30.
[48] F. Xue, Y. Si, M. Wang, M. Liu, L. Guo, Toward efficient photocatalytic pure water splitting for simultaneous H_2 and H_2O_2 production, Nanomater. Energy 62 (2019) 823–831.
[49] X. Wang, W. Fang, S. Yang, P. Liu, H. Zhao, H. Yang, Structure disorder of graphitic carbon nitride induced by liquid-assisted grinding for enhanced photocatalytic conversion, RSC Adv. 4 (2014) 10676–10679.
[50] Q. Han, Z. Cheng, B. Wang, H. Zhang, L. Qu, Significant enhancement of visible-light-driven hydrogen evolution by structure regulation of carbon nitrides, ACS Nano 12 (2018) 5221–5227.
[51] D. Zhao, C. Dong, B. Wang, C. Chen, Y. Huang, Z. Diao, S. Li, L. Guo, S. Shen, Synergy of dopants and defects in graphitic carbon nitride with exceptionally modulated band structures for efficient photocatalytic oxygen evolution, Adv. Mater. 31 (2019) 1903545–1903554.
[52] J. Chen, C. Dong, D. Zhao, Y. Huang, X. Wang, L. Samad, L. Dang, M. Shearer, S. Shen, L. Guo, Molecular design of polymer heterojunctions for efficient solar–hydrogen conversion, Adv. Mater. 29 (2017) 1606198–1606207.
[53] D. Zhao, J. Chen, C. Dong, W. Zhou, Y. Huang, S. Mao, L. Guo, S. Shen, Interlayer interaction in ultrathin nanosheets of graphitic carbon nitride for efficient photocatalytic hydrogen evolution, J. Catal. 352 (2017) 491–497.
[54] Y. Zheng, Y. Jiao, Y. Zhu, L. Li, Y. Han, Y. Chen, A. Du, M. Jaroniec, S. Qiao, Hydrogen evolution by a metal-free electrocatalyst, Nat. Commun. 5 (2014) 1–8.
[55] C. Cheng, S. Zong, S. Shi, F. Xue, Y. Zhang, X. Guan, B. Zheng, J. Deng, L. Guo, Facile preparation of nanosized MoP as cocatalyst coupled with g-C_3N_4 by surface bonding state for enhanced photocatalytic hydrogen production, Appl. Catal. B Environ. 265 (2020) 118620–118628.
[56] X. Ma, Y. Lv, J. Xu, Y. Liu, R. Zhang, Y. Zhu, A strategy of enhancing the photoactivity of g-C_3N_4 via doping of nonmetal elements: a first-principles study, J. Phys. Chem. C 116 (2012) 23485–23493.
[57] Z. Wang, J. Xu, H. Zhou, X. Zhang, Facile synthesis of Zn(II)-doped g-C_3N_4 and their enhanced photocatalytic activity under visible light irradiation, Rare Met. 38 (2019) 459–467.
[58] D. Ren, Z. Liang, Y. Ng, P. Zhang, Q. Xiang, X. Li, Strongly coupled 2D-2D nanojunctions between P-doped Ni_2S (Ni_2SP) cocatalysts and CdS nanosheets for efficient photocatalytic H_2 evolution, Chem. Eng. J. 390 (2020) 124496.
[59] D. Zhang, B. Mao, D. Li, Y. Liu, F. Li, W. Dong, T. Jiang, W. Shi, 0D/2D Z-scheme heterojunctions of Zn-$AgIn_5S_8$ QDs/α-Fe_2O_3 nanosheets for efficient visible-light-driven hydrogen production, Chem. Eng. J. 417 (2021) 128275.
[60] V. Lau, I. Moudrakovski, T. Botari, S. Weinberger, M. Mesch, V. Duppel, J. Senker, V. Blum, B. Lotsch, Rational design of carbon nitride photocatalysts by identification of cyanamide defects as catalytically relevant sites, Nat. Commun. 7 (2016) 12165–12174.
[61] J. Fu, B. Zhu, C. Jiang, B. Cheng, W. You, J. Yu, Hierarchical porous O-doped g-C_3N_4 with enhanced photocatalytic CO_2 reduction activity, Small 13 (2017) 1603938–1603946.
[62] W. Tu, Y. Zhou, Q. Liu, S. Yan, S. Bao, X. Wang, M. Xiao, Z. Zou, An in situ simultaneous reduction-hydrolysis technique for fabrication of TiO_2-graphene 2D sandwich-like hybrid nanosheets: graphene-promoted selectivity of photocatalytic-driven hydrogenation and coupling of CO_2 into methane and ethane, Adv. Funct. Mater. 23 (2013) 1743–1749.
[63] X. Chen, R. Shi, Q. Chen, Z. Zhang, W. Jiang, Y. Zhu, T. Zhang, Three-dimensional porous g-C_3N_4 for highly efficient photocatalytic overall water splitting, Nanomater. Energy 59 (2019) 644–650.
[64] Fenghua Li, Yanhong Liu, Baodong Mao, Longhua Li, Hui Huang, Dongqi Zhang, Weixuan Dong, Zhenhui Kang, Weidong Shi, Carbon-dots-mediated highly efficient hole transfer in I-III-VI quantum dots for photocatalytic hydrogen production, Appl. Catal. B Environ. 292 (2021) 120154.
[65] G. Liu, T. Wang, H. Zhang, X. Meng, D. Hao, K. Chang, P. Li, T. Kako, J. Ye, Nature-inspired environmental "phosphorylation" boosts photocatalytic H_2 production over carbon nitride nanosheets under visible-light irradiation, Angew. Chem. Int. Ed. 54 (2015) 13561–13565.
[66] X. Wang, C. Zhou, R. Shi, Q. Liu, G.I.N. Waterhouse, L. Wu, C. Tung, T. Zhang, Supramolecular precursor strategy for the synthesis of holey graphitic carbon nitride nanotubes with enhanced photocatalytic hydrogen evolution performance, Nano Res 12 (2019) 2385–2389.